BMC Bioinformatics

RESEARCH

Open Access

BDDN: bayesian dynamic differential network analysis in cancer proteomics

Juan Kim[1†], Doyeon Lee[2†], Jina Park[2,3], Ick Hoon Jin[2,3*] and Min Jin Ha[4,5*]

[†]Juan Kim and Doyeon Lee have contributed equally to this work.

*Correspondence:
Ick Hoon Jin
ijin@yonsei.ac.kr
Min Jin Ha
mjha@yuhs.ac
[1]Department of Biostatistics and Computing, Yonsei University, 50 Yonsei-ro, Seodaemungu, Seoul 03722, Republic of Korea
[2]Department of Statistics and Data Science, Yonsei University, 50 Yonsei-ro, Seodaemungu, Seoul 03722, Republic of Korea
[3]Department of Applied Statistics, Yonsei University, 50 Yonsei-ro, Seodaemungu, Seoul 03722, Republic of Korea
[4]Biohealth Data Science, Graduate School of Transdisciplinary Health Science, Yonsei University, 50 Yonsei-ro, Seodaemungu, Seoul 03722, Republic of Korea
[5]Department of Biohealth Data Science, Yonsei University, 50 Yonsei-ro, Seodaemungu, Seoul 03722, Republic of Korea

Abstract

Motivation Cancer progression and treatment responses are governed by intricate and dynamic molecular interactions. Although differential network analysis offers considerable potential for identifying condition-specific changes in protein-protein interactions, existing methods primarily rely on static comparisons between groups and do not adequately model underlying biological dynamics. This limitation restricts the ability to detect gradual and complex molecular responses to therapeutic interventions.

Results We propose a Bayesian dynamic differential network model to infer time-resolved changes in protein-protein interactions. Applied to cancer proteomics data, our approach captures gradual shifts in differential protein-protein interactions between experimental groups that standard group-based approaches fail to detect. The inferred differential networks reveal protein pairs with time-varying interaction patterns between groups, highlighting critical changes associated with drug response. Subsequent analyses, including functional clustering and hub identification, uncover distinct trajectories among differential edges and pinpoint key proteins that mediate pivotal transitions in the dynamic structure of the differential networks.

Conclusions The proposed Bayesian dynamic differential network model successfully characterizes temporal variations in protein–protein interactions following drug intervention. The method uncovers time-dependent interaction patterns that differ between experimental groups, providing enhanced insights into drug-induced molecular mechanisms. This framework facilitates the identification of critical regulatory proteins and demonstrates broad applicability across diverse time-course omics investigations.

Keywords Cancer proteomics, Protein-protein interaction, Dynamic differential network, Bayesian precision regression model

Introduction

In proteomics, functional relationships extend beyond direct protein-protein interactions, encompassing their coordinated roles within biological pathways. Proteins within cells operate as interconnected elements of complex networks that regulate critical processes such as signal transduction, metabolism, and the cell cycle [1, 2]. Investigating these functional relationships, especially their temporal dynamics, allows researchers

to understand how specific proteins influence broader biological functions [3]. Such a system-level perspective of protein dynamics is essential for elucidating disease mechanisms and advancing drug development strategies [4].

In cancer research, the system-level approach is valuable, as dysregulation of protein-interaction networks underlies cancer initiation and progression [5]. By understanding these network perturbations, researchers can pinpoint targeted therapeutic interventions, such as PARP inhibitors for DNA repair defects and biomarker development for the prediction of treatment, ultimately deepening our understanding of cancer biology [6]. These complex processes drive cancer development and progression through temporally evolving alterations in protein abundance, structures, and interactions [7]. In particular, dynamic changes in phosphorylation status and protein-protein interactions offer key insights into oncogenic signaling and regulatory mechanisms [8, 9]. Studying differences in protein-protein interactions between tumor and normal cells has revealed disease-specific alterations in protein networks [10, 11]. Moreover, tracking the temporal evolution of these protein-protein interactions provides deeper insights into cancer progression mechanisms and potential therapeutic targets [12]. Differential network analysis has emerged as a powerful strategy to uncover critical protein complexes and signaling pathways involved in tumorigenesis [13, 14], and has shown promise for informing both cancer prevention and treatment strategies [15].

A differential network maps changes in molecular connectivity and structure between two or more networks representing molecular interactions under different biological conditions. In biological contexts, these networks often represent biomolecular interactions, where nodes signify genes or proteins, and edges indicate their physical or functional relationships [16]. Researchers can identify crucial perturbations in molecular interactions by comparing networks from distinct biological states, such as healthy and diseased tissues [17]. This approach has proven particularly effective in cancer research, where it has been applied to identify differences in gene expression and epigenetic modifications, including DNA methylation, between normal and tumor samples [18]. In proteomics, differential network analysis reveals dynamic shifts in protein expression and interaction patterns under biological conditions. Special attention is often given to changes in hub nodes and pathways, as these alterations often identify key disease regulators [19, 20]. Ultimately, understanding such network dynamics enhances our understanding of disease mechanisms and facilitates the development of more precise targeted therapies.

To construct and analyze differential networks, various approaches have been developed. Early methods focused on comparing correlation-based metrics between networks. Correlation differences between genes have been tested to identify changes in direct coexpression relationships across groups [21, 22]. More recently, Gaussian graphical models have been employed to estimate group-specific networks and differences between networks are used to construct differential networks [23, 24]. These approaches provide more refined information by eliminating indirect associations that can confound correlation-based methods. However, these approaches typically compare static network snapshots between discrete conditions without accounting for the continuous evolution of network structures over time.

Accurately modeling protein-protein interaction (PPI) networks and their temporal dynamics is critical for understanding cancer biology and advancing precision medicine.

Differential network analysis has previously been applied to longitudinal gene expression data to identify temporally distinct regulatory patterns in response to perturbations [25]. In this approach, the time series is used in its entirety to construct static co-expression networks for treatment and control groups, and the resulting differential network is then interpreted using community detection and time-course visualization. Additionally, time-varying differential network models have been proposed to uncover dynamic rewiring of networks across various stages of cancer progression [26], where differential networks are estimated jointly across consecutive time points using temporally structured regularization, enabling the capture of both stage-specific and shared regulatory changes over time. However, existing approaches present key limitations. First, most methods treat time as a set of discrete stages rather than modeling it as a continuous covariate, which hinders the ability to predict gradual changes in network structure over time. Second, many frameworks do not explicitly separate condition-specific effects from general temporal trends, making it difficult to distinguish treatment-induced changes from time-driven variability. These limitations restrict the ability to fully characterize dynamic, condition-specific rewiring of biological networks.

To address these limitations, we propose Bayesian dynamic differential network model to investigate time-varying differential patterns between sample groups. Our approach leverages Bayesian Markov Chain Monte Carlo (MCMC) sampling to robustly quantify uncertainty in network estimation, thereby enhancing the reliability of differential network inference and enabling biologically interpretable insights into the dynamic evolution of protein interactions throughout cancer progression and drug administration.

We applied our model to data from the Cancer Perturbed Proteomics Atlas (CPPA) project [27, CPPA] to estimate temporal changes in protein networks between control and treatment groups. The CPPA dataset offers comprehensive protein response measurements generated through reverse phase protein array (RPPA) technology [28]. As a proof of concept, we focused on breast cancer, a well-characterized cancer type with abundant available data. Specifically, for the treatment group, we analyzed samples treated with lapatinib, a dual tyrosine kinase inhibitor targeting HER2 and EGFR [29]. LAPATINIB is essential in managing HER2-positive breast cancer, particularly among patients resistant to trastuzumab [30]. By disrupting critical signaling pathways involved in tumor progression [31], lapatinib provides a biologically meaningful context to investigate differential protein-protein interactions between the control and treatment conditions.

Materials and methods

BDDN model

We define the dynamic differential network as $G(t) = (V, E(t))$, where the time-constant vertex set $V = \{1, \ldots, p\}$ corresponds to the proteins, and the time-dependent edge set $E(t)$ that represents differential protein-protein interactions among experimental conditions at time t. In our framework, edges are defined based on partial correlations, which capture the conditional dependencies between protein pairs while controlling for the effects of all other proteins. The construction of $G(t)$ involves three main steps: (1) estimation of group- and time-specific partial correlation matrices, (2) calculation of differential scores quantifying differences between groups at each time

point, and (3) functional clustering of the resulting differential score trajectories over time. A detailed step-by-step procedure is provided below Fig. 1.

Step 1 dynamic precision regression

Suppose that we have protein expression data for n samples. Let $\mathrm{Y} = (\mathrm{y}_1, \cdots, \mathrm{y}_n)^{\mathrm{T}}$ be the $n \times p$ matrix, where $\mathrm{y}_i \in \mathbb{R}^p$ indicates expressions of p proteins for the sample i. Let $\mathrm{X} = (\mathrm{x}_1, \cdots, \mathrm{x}_n)^{\mathrm{T}}$ be the $n \times q$ design matrix. The ith row of X, denoted as $\mathrm{x}_i \in \mathbb{R}^q$, is a $q \times 1$ covariate vector for the sample i.

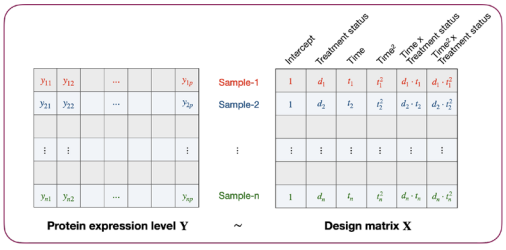

(a) Input

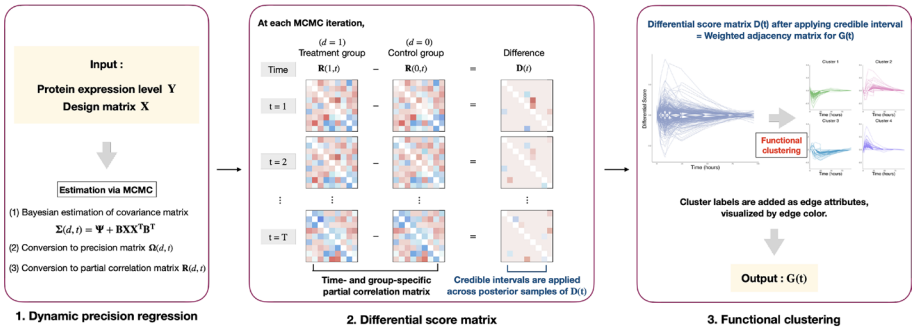

(b) Model Estimation Steps

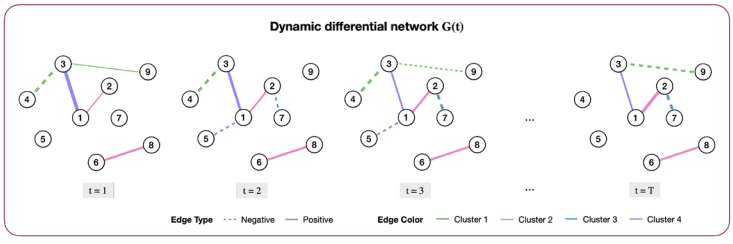

(c) Output

Fig. 1 Flowchart of the model **a** Input: The model takes as input the protein expression level data Y and the corresponding design matrix X, which includes experimental conditions such as treatment status and time-related covariates. **b** Model Estimation Steps: *Step 1. Dynamic precision regression:* A precision regression model is employed to capture covariance structures that vary across treatment status and time points. Estimated covariance matrices are converted to precision matrices and subsequently to partial correlation matrices. Model parameters are estimated using MCMC sampling, generating time- and group-specific partial correlation matrices for each posterior sample. *Step 2. Differential score matrix:* At each time point, the difference between partial correlation matrices of treatment and control groups is computed as $\mathrm{D}(t) = \mathrm{R}(1,t) - \mathrm{R}(0,t)$ for each posterior sample. These posterior samples of $\mathrm{D}(t)$ are used to construct credible interval-based thresholds, producing a differential score matrix that quantifies time-specific differences between groups. *Step 3. Functional clustering:* The temporal trajectory of each edge in $\mathrm{D}(t)$-that is, the time series of differential scores for each protein pair-is treated as functional data and grouped using functional clustering methods. Resulting cluster assignments are encoded as edge colors in the dynamic differential network $G(t)$. **c** Output: The final output is a dynamic differential network $G(t)$, where nodes represent proteins and edges indicate differential interactions between the treatment and control groups. Solid and dashed lines denote the sign of the differential score (positive and negative, respectively). Edge width is proportional to interaction strength (the absolute value of the differential score), and edge color reflects the results of functional clustering

We consider a multivariate regression framework with random effects [32],

$$\mathrm{y}_i = \mathrm{A}\mathrm{x}_i + \gamma_i \mathrm{B}\mathrm{x}_i + \boldsymbol{\epsilon}_i, \quad i = 1, \cdots n \tag{1}$$

where A and $\mathrm{B} \in \mathbb{R}^{p\times q}$ are coefficient matrices to be estimated, $\gamma_i \in \mathbb{R}$ is a random effect and $\boldsymbol{\epsilon}_i \in \mathbb{R}^p$ is a p-dimensional error vector, which are given as

$$\gamma_i \overset{\text{iid}}{\sim} N(0,1), \quad \boldsymbol{\epsilon}_i \overset{\text{iid}}{\sim} \mathrm{MVN}(0, \boldsymbol{\Psi}).$$

These distributional assumptions on random effects and error terms induce the normal distribution on y_i as

$$\mathrm{y}_i \sim \mathrm{MVN}(\mathrm{A}\mathrm{x}_i, \boldsymbol{\Sigma}_{\mathrm{x}_i}) \quad \forall i = 1, \cdots, n$$

where

$$\boldsymbol{\Sigma}_{\mathrm{x}_i} = \mathrm{Cov}[\mathrm{y}_i|\mathrm{x}_i] = \mathrm{B}\mathrm{x}_i\mathrm{x}_i^{\mathrm{T}}\mathbf{B}^{\mathbf{T}} + \boldsymbol{\Psi}. \tag{2}$$

Extending this to all observations, the covariance structure becomes $\boldsymbol{\Sigma}_{\mathrm{X}} = \mathrm{Cov}[\mathrm{Y}|\mathrm{X}] = \boldsymbol{\Psi} + \mathrm{B}\mathrm{X}\mathbf{X}^{\mathbf{T}}\mathbf{B}^{\mathbf{T}}$, where the regression coefficient matrix $\mathrm{B} = [B_{ab}]_{p\times q}$ encodes the effects of covariates on the covariance structure, and $\boldsymbol{\Psi}$ denotes the baseline covariance matrix that remains independent of the design matrix X. In our inferential framework of differential networks, we focus on estimating the covariance function $\boldsymbol{\Sigma}_{\mathrm{X}}$ as a function of covariates X via the coefficient B and the baseline covariance matrix $\boldsymbol{\Psi}$, rather than modelling the mean of y_i.

Specifically in our application, we consider $\mathrm{x}_i = (1, d_i, t_i, t_i^2, d_i \cdot t_i, d_i \cdot t_i^2)^{\mathrm{T}}$, where d_i is a binary indicator for our two experimental conditions, with $d_i = 0$ for the control group and $d_i = 1$ for the treatment group. The inclusion of the squared-time term improves the flexibility of the model in capturing curvature in temporal trends, enabling a more accurate representation of nonlinear interaction dynamics between proteins under experimental conditions. The interaction terms $d_i \cdot t_i$ and $d_i \cdot t_i^2$ enable the model to capture how time effects differ between the treatment and control groups, both in linear and nonlinear ways.

For notational convenience and to emphasize application-specific clarity, we denote the covariance matrix as $\boldsymbol{\Sigma}(d,t)$ on treatment status *d* and time *t* instead of the generic $\boldsymbol{\Sigma}_{\mathrm{X}}$, explicitly indicating its dependence on treatment status *d* and time *t*.

Given the covariance regression model in Eq.2), we aim to estimate the posterior distributions of the model parameters that characterize the time- and group-specific covariance structure $\boldsymbol{\Sigma}(d,t)$. To perform a Bayesian estimation, we adopt a Metropolis-Hastings-within-Gibbs sampling algorithm. At each iteration of the Gibbs sampler, the parameters $\boldsymbol{\Psi}$ and B are sequentially updated, along with random effects γ_i. We assume a matrix-normal prior on $\mathrm{C} = (\mathrm{A}, \mathrm{B})$ and an inverse-Wishart prior on $\boldsymbol{\Psi}$, enabling tractable posterior updates. The Gibbs sampler iteratively samples random effects γ_i, the coefficient matrices A, B, and $\boldsymbol{\Psi}$. At each iteration, posterior samples of $\boldsymbol{\Psi}$ and $\boldsymbol{B}$ are used to compute the group- and time-specific covariance matrices $\boldsymbol{\Sigma}(d,t)$, followed by precision and partial correlation matrices as described below. Full details of the MCMC implementation, including prior specification and sampling steps, are provided in Supplementary Section 2. Details on computational runtime across varying number of proteins are provided in Supplementary Section 7.

These covariance matrices capture marginal associations among protein expression levels but do not distinguish between direct and indirect relationships. To identify direct conditional dependencies, we convert each posterior sample of the covariance matrix into a precision matrix $\mathbf{\Omega}(d,t) = \mathbf{\Sigma}(d,t)^{-1}$ and provides a representation of conditional dependencies between proteins after adjusting for all others. The time- and group-specific precision matrix $\mathbf{\Omega}(d,t)$ is derived using the following mathematical formulation [33]:

$$\mathbf{\Omega}(d,t) = \mathbf{\Psi}^{-1} - \frac{1}{1+\kappa(\mathrm{X})}\mathbf{\Psi}^{-1}\mathrm{BX^TXB^T}\mathbf{\Psi}^{-1},$$

where $\kappa(\mathrm{X}) = \mathrm{tr}(\mathrm{BXX^TB^T}\mathbf{\Psi}^{-1})$ represents the trace normalization term. The conditional dependencies represented by $\mathbf{\Omega}(d,t)$ reflect the partial correlations between protein pairs after accounting for the influence of all other proteins in the network.

We provide a detailed characterization of the group-specific precision matrix $\mathbf{\Omega}(d,t)$ through explicit examination of its diagonal and off-diagonal components. For any specified treatment group $d \in \{0,1\}$ and time point *t*, we establish the group-specific covariate vector as

$$\mathrm{x}_i^{(d)} = \begin{cases} (1,0,t_i,t_i^2,0,0)^T, & \text{for the control group } (d=0), \\ (1,1,t_i,t_i^2,t_i,t_i^2)^T, & \text{for the treatment group } (d=1). \end{cases}$$

We establish the notation for the group-specific precision matrices as $\mathbf{\Omega}(0,t) = [\omega_{ab}^{(0)}]_{p\times p}$ and $\mathbf{\Omega}(1,t) = [\omega_{ab}^{(1)}]_{p\times p}$ for control and treatment groups, respectively. The diagonal elements $\omega_{aa}^{(d)}$ quantify the marginal precision of individual protein *a*, while off-diagonal elements $\omega_{ab}^{(d)}$ for $a \neq b$ measure the conditional dependence between protein pairs given all other proteins within group $d \in \{0,1\}$, under the group $d \in \{0,1\}$.

To simplify the expression of each matrix element, we introduce the transformation vector $\mathrm{z}_i^{(d)} = \mathbf{\Psi}^{-1}\mathrm{Bx}_i^{(d)}$ and express the entries of the precision matrix as follows:

$$\omega_{aa}^{(d)} = (\mathbf{\Psi}^{-1})_{aa} - \frac{(z_{ia}^{(d)})^2}{1+\kappa_i^{(d)}}, \quad \omega_{ab}^{(d)} = (\mathbf{\Psi}^{-1})_{ab} - \frac{z_{ia}^{(d)} z_{ib}^{(d)}}{1+\kappa_i^{(d)}},$$

where $\kappa_i^{(d)} = (\mathrm{z}_i^{(d)})^T\mathbf{\Psi}\mathrm{z}_i^{(d)}$. Each element $z_{ia}^{(d)}$ of $\mathrm{z}_i^{(d)}$ is given by

$$z_{ia}^{(0)} = \sum_{k=1}^{p}(\mathbf{\Psi}^{-1})_{ak}\left(B_{k1} + B_{k3}t_i + B_{k4}t_i^2\right),$$
$$z_{ia}^{(1)} = \sum_{k=1}^{p}(\mathbf{\Psi}^{-1})_{ak}\left(B_{k1} + B_{k2} + (B_{k3}+B_{k5})t_i + (B_{k4}+B_{k6})t_i^2\right).$$

The off-diagonal element $\omega_{ab}^{(d)}$ $(a \neq b)$ represents a treatment- and time-dependent adjustment to the baseline network structure. The baseline conditional dependence between proteins *a* and *b* is captured by $(\mathbf{\Psi}^{-1})_{ab}$, after controlling for all other proteins in the network. The second term, $-\frac{z_{ia}^{(d)} z_{ib}^{(d)}}{1+\kappa_i^{(d)}}$, reflects how this dependence is modulated by treatment assignment and time point through the projected covariate effect vector $\mathrm{z}_i^{(d)} = \mathbf{\Psi}^{-1}\mathrm{Bx}_i^{(d)}$. In this formulation, the covariate vector incorporates time-dependent

changes in protein interactions for both control and treatment groups, while treatment-induced alterations are selectively applied to the intervention group through the coefficient terms associated with $d = 1$.

We then construct the partial correlation matrix $\mathrm{R}(d,t) = [r_{ab}^{(d,t)}]_{p\times p}$ from the estimated precision matrix. The partial correlation coefficient quantifies the strength of the direct association between two proteins after controlling for the linear effects of all other proteins in the system. This coefficient is computed through the standardization of the precision matrix elements as follows:

$$r_{ab}^{(d,t)} = -\frac{\omega_{ab}^{(d,t)}}{\sqrt{\omega_{aa}^{(d,t)}\omega_{bb}^{(d,t)}}}.$$

This provides a more intuitive understanding of direct relationships between proteins, independent of their scale, making it more suitable for network construction. The partial correlation matrix is computed from each posterior sample of the precision matrix at each MCMC iteration.

Step 2 Differential score matrix $\mathrm{D}(t)$

Based on the posterior samples of partial correlation matrices, we compute a differential score matrix at each time point for every posterior sample by subtracting the partial correlation matrices of the control group $(d = 0)$ from that of the treatment group $(d = 1)$:

$$\mathrm{D}(t) = \mathrm{R}(1,t) - \mathrm{R}(0,t). \tag{3}$$

This results in a collection of differential score matrices at each time point for downstream analysis.

For each element (*a*, *b*) of the matrix at time *t*, we construct a credible interval $\mathrm{CI}_{ab}^{(t)}$ across posterior samples. If the interval includes zero, the corresponding entry is set to zero; otherwise, the posterior mean is assigned. The final differential score matrix $\mathrm{D}(t)$ is defined elementwise as

$$\mathrm{D}_{ab}(t) = \begin{cases} 0, & \text{if } 0 \in \mathrm{CI}_{ab}^{(t)} \\ \frac{1}{S}\sum_{s=1}^{S}\left(r_{ab}^{(1,t,s)} - r_{ab}^{(0,t,s)}\right), & \text{otherwise} \end{cases},$$

where $r_{ab}^{(d,t,s)}$ denotes the (*a*, *b*)-th element of the partial correlation matrix for group *d* at time *t*, obtained from the *s*-th MCMC iteration. The resulting matrix $\mathrm{D}(t)$ serves as a proxy for the weighted adjacency matrix of the dynamic differential network $G(t)$ with each entry representing the magnitude and direction of treatment-induced changes in protein-protein interactions over time. In this matrix, non-significant differential edge scores are set to zero, and only significant changes are retained as posterior mean values.

Step 3 Functional clustering

Leveraging the dynamic differential network (DDN) proxy, $\mathrm{D}(t)$, estimated via our Bayesian framework, we introduce an edge-labeling method to characterize time-varying mechanisms in the network. Specifically, we perform functional clustering analysis on the differential score trajectories to classify edges (protein pairs) exhibiting similar temporal dynamics.

By treating each trajectory $\{\mathrm{D}_{ab}(t), t \in \mathcal{T}\}$ as a functional data object, we identify protein pairs that follow comparable patterns of differential connectivity over time. The resulting cluster labels are incorporated as edge attributes in the network and visualized using edge color, providing a more interpretable representation of the dynamic differential network $G(t)$.

We used functional principal component analysis (FPCA) [34] to decompose time-varying differential score trajectories into a set of basis functions. The rationale for selecting this approach is detailed in Supplementary Section 3.4. For each pair of proteins $\{a, b\}$, the differential score trajectory $\mathrm{D}_{ab}(t)$ can be represented as a linear combination of basis functions $\mathbf{\Phi} = \{\phi_1, \cdots, \phi_L\}$, where L is the number of basis functions. Specifically, it is given as

$$\mathrm{D}_{ab}(t) = \sum_{\ell=1}^{L} \alpha_{(ab)\ell}\phi_\ell(t), \tag{4}$$

where $\alpha_{(ab)\ell}$ denotes the FPCA score corresponding to each basis function. The coefficient $\alpha_{(a,b)\ell}$ quantifies how strongly the differential interaction between proteins a and b aligns with the ℓ-th principal temporal pattern. We implement this decomposition using quadratic B-splines [35] as our basis functions, which provide the necessary flexibility to capture temporal dynamics. The number of basis functions L is determined by placing knots at regularly spaced time intervals. We then group protein-protein interactions with similar temporal differential patterns by applying the k-means clustering to the FPCA scores. This computationally efficient and interpretable method requires the selection of the optimal number of clusters k, which we determine using the elbow method based on the sum of squares within the cluster in a scree plot. This approach effectively classifies protein-protein interactions according to their temporal differential patterns.

Each functional group identifies a distinct temporal pattern of differential protein-protein interactions over time, providing information on the dynamic modulation of the protein interactome in response to treatment. From these temporal signatures, we systematically construct the time-dependent edge set $E(t)$ comprising protein-protein interactions that demonstrate statistically significant differential connectivity conforming to the identified temporal profiles. The cluster label assigned to each interaction is incorporated as an edge attribute in the network and is visualized using edge color in the final representation of $G(t)$. This edge set, combined with the protein vertex set V, constitutes the dynamic differential network $G(t) = (V, E(t))$, which comprehensively characterizes the temporal evolution of treatment-induced alterations in the protein-protein interaction architecture. Subsequent network analysis of cluster-specific subnetworks facilitates the identification of topologically important interactions, regulatory hubs, and temporally coordinated protein modules, potentially revealing the mechanistic cascades that mediate observed treatment effects and providing information on the underlying biological processes.

Identification of hub proteins

To identify hub proteins that play central roles in the dynamic differential network $G(t)$, we use the final differential score matrix $\mathrm{D}(t)$, which serves as the adjacency matrix for

$G(t)$. We compute three centrality measures (degree, betweenness, and eigenvector centrality) to quantify different aspects of protein influence within $G(t)$. Degree centrality measures local connectivity and is defined as $C_D(i) = \sum_j \mathrm{D}_{ij}(t)$, the number of proteins directly connected to protein *i*. Betweenness centrality captures a protein's role as a bridge between other proteins and is calculated as $C_B(i) = \sum_{s \neq i \neq t} \frac{\sigma_{st}(i)}{\sigma_{st}}$, where σ_{st} is the total number of shortest paths between proteins *s* and *t*, and $\sigma_{st}(i)$ is the number of those paths passing through protein *i*. Eigenvector centrality reflects both the quantity and quality of connections, computed as $C_E(i) = \frac{1}{\lambda} \sum_j \mathrm{D}_{ij}(t) C_E(j)$, where λ is the leading eigenvalue of $\mathrm{D}(t)$ and $C_E(i)$ accounts for the importance of neighboring proteins. For each centrality metric, we construct scree plots and apply the elbow method to systematically identify a threshold for selecting influential proteins. Proteins exceeding this threshold are classified as hub proteins, representing the central nodes in the dynamic differential network.

Data

Our analysis utilizes data from the Cancer Perturbed Proteomics Atlas [27, CPPA], a comprehensive project conducted at the University of Texas MD Anderson Cancer Center that maps changes in protein expression in cancer cell lines after drug treatments. Using RPPA technology, researchers measure both protein quantities and modifications in samples from cultured cells. This cost-effective and high-throughput method uses specific antibodies to analyze protein networks and signaling pathways crucial to cancer development [36]. This dataset comprises protein expression measurements obtained under various experimental conditions, including different compounds (drugs), cell lines, and durations of treatment.

In our application, we focus on LAPATINIB-treated breast cancer cell line samples as the treatment group. We used DMSO-treated samples as our control group, as DMSO is a standard vehicle control in biological experiments [37, 38]. Protein expression levels in each group were measured at multiple irregular time points, with time points varying between samples. This temporal structure enables the analysis of dynamic changes in protein-protein interactions over time.

Our study analyzed expression data for 78 proteins in 933 samples, after excluding proteins with missing values across all 933 samples. In total, our analysis included 474 LAPATINIB-treated samples and 459 DMSO-treated control samples, spanning 17 irregularly spaced time points ranging from 0 to 96 h. The detailed data preprocessing procedure is provided in Supplementary Section 1.

Results

We applied our method BDDN to the control and LAPATINIB-treated groups to infer dynamic differential networks. The BDDN model was implemented using MCMC sampling with 200,000 iterations, a thinning interval of 10, and a burn-in period of 5,000. To further investigate the robustness of the BDDN, we performed additional analyses by varying the sample size and prior settings. The results demonstrate that the key estimates remain consistent and robust across these varying conditions (see Supplementary Sections 5.1 and 5.2). Convergence of B, $\mathbf{\Psi}$, and $\mathbf{\Sigma}_{\mathrm{x}_i}$ was evaluated using trace plots as presented in Supplementary Section 2.2. Network edges were identified by selecting differential scores whose 99.5% credible intervals excluded zero, which indicates

statistically significant associations. These networks captured LAPATINIB-induced changes in protein-protein interactions over time. By analyzing these, we aim to uncover the temporal mechanisms underlying its therapeutic effects. As a further validation, we analyzed CPPA skin cancer cell lines under the MEK inhibitor trametinib and observed consistent dynamic rewiring and hub shifts (e.g., MEK1, Bax, Bim), supporting the generalizability of BDDN (see Supplementary Section 3.5).

Figure 2 illustrates the temporal changes in edge count of the dynamic differential network. We observed that the edge count peaked at 8 h, suggesting that the effect of LAPATINIB on protein-protein interactions is most pronounced at this time point. These findings align with previous biological research that demonstrates the time-dependent effects of LAPATINIB on various molecular pathways. For example, Tang et al. [39] reported that LAPATINIB induces `p27(Kip1)` expression in HER2-positive breast cancer cells in a dose- and time-dependent manner, with a significant increase in `p27` levels occurring within 24 - 48 h after treatment. Similarly, Leung et al. [40] observed that LAPATINIB induces the expression of `NRG1` mRNA in `SK-BR-3` and `BT-474` breast cancer cells approximately 8 h after treatment, highlighting the temporal specificity of LAPATINIB's impact on key signaling pathways. These studies support our observation that the molecular effects of LAPATINIB evolve over time, corroborating the temporal patterns revealed in our differential network analysis.

We identified hub proteins in differential networks at 8, 24 and 48 h based on the three different centrality measures: degree, betweenness, and eigenvector centrality. The scree plots displayed in Figure 7 of Supplementary Materials of provide cutoff values to declare proteins as hubs. Table 1 and Fig. 3 presents the hub proteins identified at each time point, with key proteins involved in LAPATINIB-targeted pathways highlighted in bold. LAPATINIB targets the `HER2/EGFR` signaling pathway and its main downstream cascades, the `PI3K/AKT` and `MAPK/ERK` pathways [41, 42]. Our hub protein identification approach successfully captured proteins from these LAPATINIB-targeted pathways,

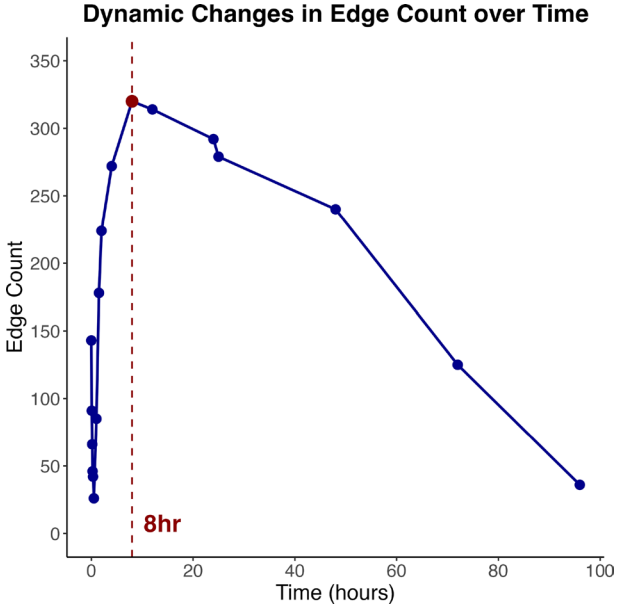

Fig. 2 Dynamic changes in edge count over time in the differential network

Table 1 Hub protein dynamics across 8, 24, and 48 h

Centrality	8hr Hubs	24hr Hubs	48hr Hubs
Degree	p27 (6), **PDK1_pS241** (6), MEK1 (4), **PTEN** (4), Chk2 (3), Cyclin-E1 (3), YAP (3)	JNK2 (5), **Akt_pT308** (4), **ER-alpha** (4), p27 (4), **PDK1_pS241** (4), **P70S6K** (3) **p70-S6K_pT389** (3), YB1_pS102 (3)	JNK2 (6), **Akt_pT308** (5), **PDK1_pS241** (4), CD31 (3), c-Kit (3), p27 (3), **p70-S6K_pT389** (3)
Betweenness	p27 (433), **PDK1_pS241** (335), Bcl-xL (294), **PTEN** (235), **P70S6K** (234), MEK1 (210)	JNK2 (68), **Akt_pT308** (38), p27 (36), **PDK1_pS241** (27), **p70-S6K_pT389** (23)	JNK2 (102.9), **Akt_pT308** (64.4), **PDK1_pS241** (55.7), **p70-S6K_pT389** (30)
Eigenvector	**PTEN** (1), **P70S6K** (0.681), Chk2 (0.484), Fibronectin (0.438), **ER-alpha** (0.389)	**ER-alpha** (1), **PTEN** (0.807), **P70S6K** (0.616), PKC-alpha_pS657 (0.586)	JNK2 (1), **PDK1_pS241** (0.609), p27 (0.554), **p70-S6K_pT389** (0.524), c-Kit (0.446), **Akt_pT308** (0.430)

List of hub proteins detected at 8, 24, and 48 h based on degree, betweenness, and eigenvector centrality, derived from the final differential score matrix $\mathrm{D}(t)$ after applying the HPD interval

Hub proteins are categorized as: (1) early-only hubs (8 h only), (2) persistent hubs (8-48 h), and (3) late-emerging hubs (24 or 48 h only)

Values in parentheses represent the respective centrality scores for each protein at the corresponding time point

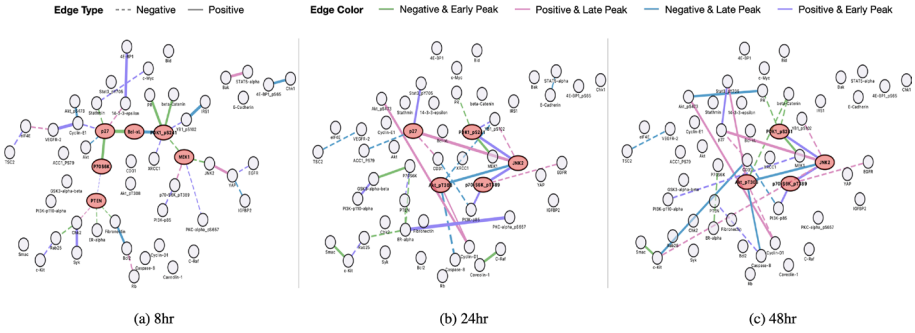

Fig. 3 Differential network at **a** 8, **b** 24, and **c** 48 h. Nodes represent proteins, and edges indicate differential interactions between the treatment and control groups. Solid and dashed lines denote the sign of the differential score (positive and negative, respectively). Edge width is proportional to the absolute value of the differential score, and edge color reflects the results of functional clustering. Hub proteins (red) and non-hub proteins (gray) are identified based on betweenness centrality, which quantifies a node's importance according to its position in network pathways

such as PTEN and PDK1-pS241, demonstrating the biological relevance of the identified network structures.

As shown in Table 1, PTEN functions as an early stage hub (8 h) within the first group. This tumor suppressor protein acts as a critical negative regulator of the PI3K/AKT pathway by catalyzing the conversion of PIP_3 to PIP_2, thereby inhibiting AKT activation [43]. When LAPATINIB inhibits HER2/EGFR activation, it significantly reduces upstream PI3K signaling, resulting in decreased PIP_3 levels. Under these conditions, PTEN amplifies the therapeutic effect by eliminating the remaining PIP_3, thus enhancing LAPATINIB's inhibition of AKT activation [44]. Given PTEN's upstream regulatory position in the PI3K/AKT pathway, its influence is most pronounced during the early response phase, consistent with our differential network analysis, which identified it as an early hub. The subsequent decline in PTEN prominence at later time points probably reflects feedback regulation mechanisms that diminish its activity after the initial response [45].

PDK1_pS241, the phosphorylated form of PDK1 in Ser241, maintained consistent activity throughout the observation period and was identified as a persistent hub. PDK1 is a central kinase downstream of PI3K that activates AKT by phosphorylation in Thr308, an essential step in the signaling cascade of AKT [43]. Importantly, autophosphorylation at Ser241 maintains PDK1 in its active conformation, allowing for rapid response to upstream signals [46]. Despite LAPATINIB-induced reduction in PIP_3 levels and subsequent attenuation of AKT and S6K activation, PDK1_pS241 retains its phosphorylation state and functional activity, allowing it to transmit signals if PI3K activity recovers [47]. This sustained activation pattern may explain why PDK1_pS241 consistently emerged as a hub across all time points in our differential network analysis.

P70-S6K and its phosphorylated form p70-S6K_pT389 (at threonine 389) were identified as late-emerging hubs. Phosphorylation of p70S6K in T389 is commonly used as a read-out for mTORC1 activity and indicates activation of the PI3K/AKT/mTOR signaling pathway [48, 49]. During initial LAPATINIB treatment, PI3K activity was suppressed, decreasing mTORC1 signaling and consequently reducing p70-S6K_pT389 levels. However, as treatment progresses, negative feedback mechanisms were alleviated, allowing alternative upstream signals - particularly insulin/IGF-1R and HER3 signaling - to partially restore PI3K activity [50]. This compensatory mechanism led to the reactivation of mTORC1 and p70S6K, especially at later time points. The emergence of p70-S6K_pT389 as a hub protein specifically at 24 and 48 h corresponded to its reactivation through these feedback relief mechanisms and alternative signaling pathways. This finding demonstrates the dynamic nature of the PI3K/AKT/mTOR pathway and underscores how feedback loops can reshape the network architecture over time.

Based on the trajectories of differential scores, the FPCA identified 5 clusters (Fig. 4). Cluster 5, shown in gray in Fig. 4a, includes protein pairs with differential scores near zero, indicating a small change and no significant differences between the control and treatment groups. Due to its negligible variation, this cluster has been excluded from the main plots, and its corresponding spaghetti plot and heatmap have been provided in Figure 8 of the Supplementary Material.

These distinct temporal patterns likely reflect the complex, feedback-rich signaling landscape modulated by LAPATINIB. Previous phosphoproteomic and kinome studies have demonstrated that LAPATINIB treatment leads to immediate pathway inhibition and delayed compensatory reactivation. For example, early suppression of AKT and ERK signaling has been shown to rebound after 24–48 h due to HER3- or FGFR-mediated feedback loops [51, 52]. Such biphasic responses correspond well to the early and late peaks observed in our clusters. Moreover, the coexistence of positively and negatively regulated edges is consistent with previous findings that LAPATINIB simultaneously downregulates multiple phosphorylation sites while upregulating specific regions (e.g., Ser/Thr clusters on HER2) [47]. This suggests that each cluster may correspond to a unique adaptation mechanism within the protein-protein interaction network, driven by the interplay of pathway inhibition and compensatory rewiring. Overall, these results highlight the value of dynamic network analysis in uncovering the temporal complexity of cellular responses to targeted therapy [53, 54].

As an external validation, we analyzed CPPA skin cancer cell lines under the MEK inhibitor trametinib and observed biologically significant hubs (e.g., MEK1, Bax, Bim), supporting the generalizability of BDDN (Supplementary Section 3.5).

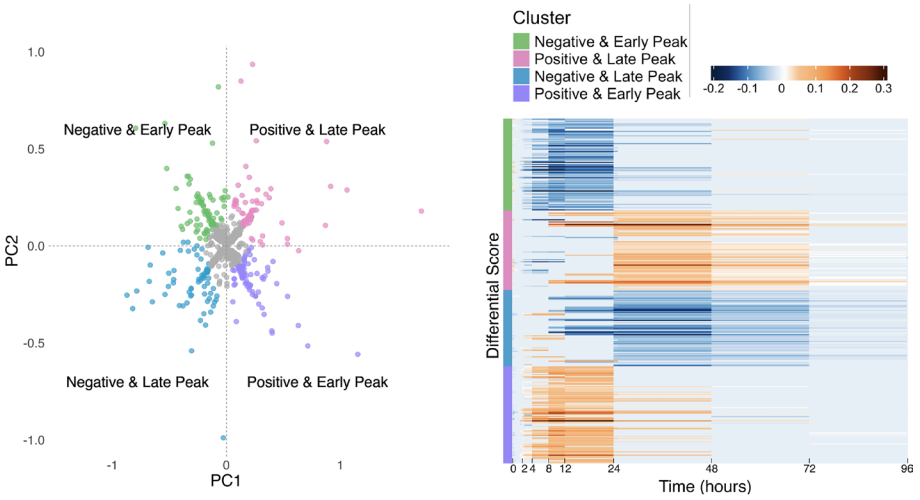

(a) Functional clustering (b) Heatmap

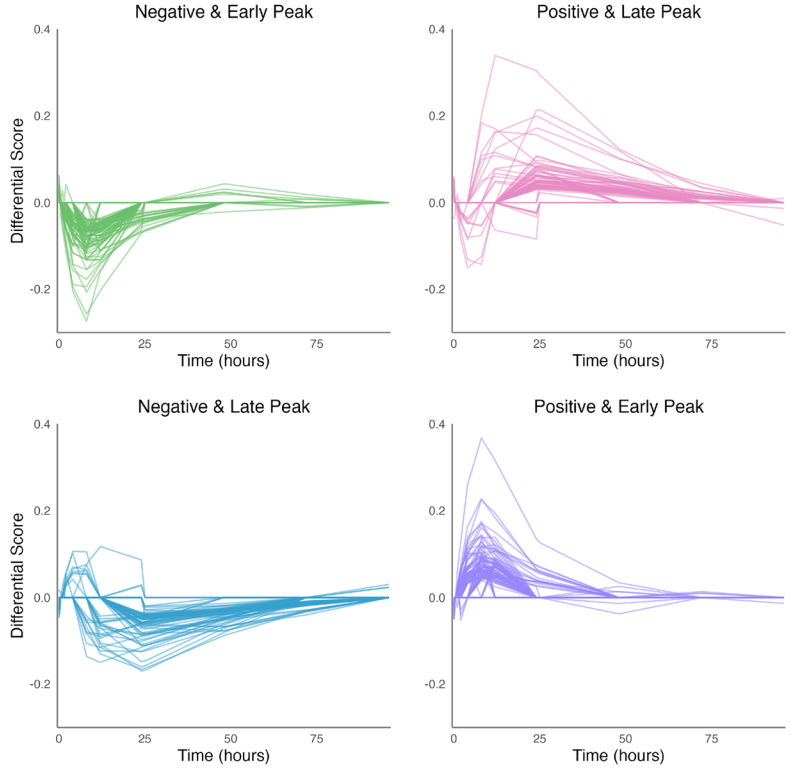

(c) Differential score

Fig. 4 Functional clustering identifies five drug-response patterns in protein interactions. Functional clustering categorized protein pairs into five clusters based on changes in partial correlation after drug treatment: Cluster 1 (Negative Change, Early Peak), Cluster 2 (Positive Change, Late Peak), Cluster 3 (Negative Change, Late Peak), Cluster 4 (Positive Change, Early Peak), and Cluster 5 (Small Change). **a** Scatter plot displaying functional clustering results. The x-axis (PC1) differentiates clusters based on correlation change direction (negative or positive), while the y-axis reflects the interaction between directionality and peak timing. **b** Heatmap of differential scores illustrating temporal changes in protein-protein interactions. Rows represent protein pairs, and columns represent time points. **c** Spaghetti plots demonstrating differential scores temporal dynamics across the five clusters. Each panel corresponds to one cluster, with individual line representing the time-dependent variation in differential scores for specific protein pairs

Simulation studies

We conducted comprehensive simulation studies to evaluate the performance of our BDDN methodology, designing the simulated data structure to closely mirror our real data analysis. The simulation included 900 total samples across 80 proteins, with sample allocation reflecting the original study design: 433 samples designated as the control group (d = 0) and 467 samples assigned to the treatment group (d = 1). Sample generation was systematically aligned with the actual sample distributions observed at each temporal measurement point in the real data analysis, ensuring that our simulation framework accurately captured the statistical properties and structural characteristics of the empirical dataset.

We assigned each sample a covariate vector $\mathrm{x}_i = (1, d_i, t_i, t_i^2, d_i \cdot t_i, d_i \cdot t_i^2)$ and the covariance matrix was constructed according to $\Sigma(d_i, t_i) = \Psi + \mathrm{B}\mathrm{x}_i\mathrm{x}_i^{\mathrm{T}}\mathrm{B}^{\mathrm{T}}$. The noise covariance matrix $\mathbf{\Psi} = \mathrm{diag}(0.1, \ldots, 0.1)$ represents the baseline variability, while the coefficient matrix $\mathrm{B} \in \mathbb{R}^{80\times 6}$ encodes the systematic effects of covariates on the covariance structure.

The coefficient matrix B captures different biological and experimental effects through its column structure. The first column $\{B_{i1} : i = 1, \ldots, p\}$ represents the intercept term for each protein, establishing the baseline covariance levels. The second column $\{B_{i2}\}$ quantifies the direct effect of the treatment group on protein interactions. The third and fourth columns $\{B_{i3}, B_{i4}\}$ model the linear and quadratic temporal effects, respectively, capturing how protein relationships evolve over time. The fifth and sixth columns $\{B_{i5}, B_{i6}\}$ represent the interaction terms between treatment status and time, allowing treatment-specific temporal dynamics to be expressed in linear and quadratic forms.

We established simulation parameters based on the posterior distributions of B estimated from our real data analysis, ensuring realistic effect sizes that reflect observed biological variation. The coefficient distributions were specified as follows: $B_{i1} \sim \mathcal{N}(0.034, 0.29^2)$ for intercept effects, $B_{i2} \sim \mathcal{N}(-0.01, 0.28^2)$ for treatment effects, $B_{i3} \sim \mathcal{N}(0.01, 0.14^2)$ and $B_{i4} \sim \mathcal{N}(0.004, 0.03^2)$ for linear and quadratic time effects, and $B_{i5} \sim \mathcal{N}(0.003, 0.09^2)$ and $B_{i6} \sim \mathcal{N}(0.001, 0.23^2)$ for treatment-time interaction effects.

We implemented this simulation framework to generate individual datasets and performed 100 independent replicates to access performance in indentifying the dynamic differential network structure $G(t)$. In each replicate, we applied the BDDN approach to estimate the differential score matrix, with performance benchmarked against the established DINGO model [55] for comparative evaluation. We quantified the performance of the method through the detection accuracy of the edge level, the construction of receiver operating characteristic (ROC) curves for each approach, and the computation of the values of the area under the curve (AUC).

As shown in Fig. 5, BDDN consistently achieved higher AUC values across all time points. The performance gap was especially evident at time points with smaller sample sizes, where DINGO tended to yield noisy and unstable estimates, whereas BDDN remained accurate and reliable. These results demonstrate the advantage of BDDN in recovering differential networks. Each ROC curve and the corresponding AUC value for all time points are provided in Figure 8 of the Supplementary Materials.

Furthermore, we have implemented an additional, independent simulation scenario designed with a distinct data-generating process, using alternative effect sizes and noise

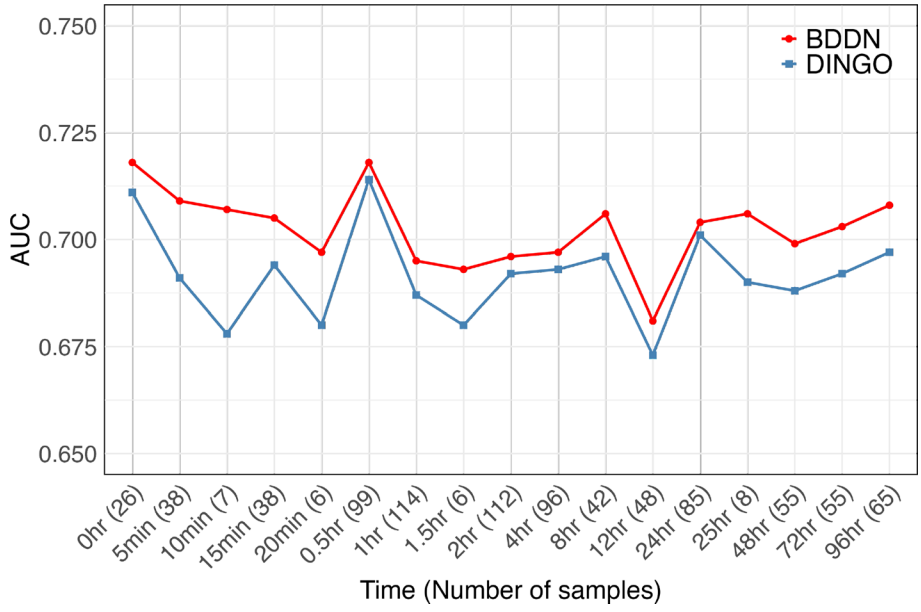

Fig. 5 Simulation results comparing the performance of BDDN and DINGO models over time. AUC values are derived from ROC curves for differential score matrix estimation. The x-axis shows time points with corresponding sample sizes. BDDN demonstrates consistently superior performance, with the most pronounced improvements occurring at time points with limited sample sizes

structures not derived from the posterior estimates. This scenario included glasso [56] to compare the performance (See Supplementary Section 4.2). The results demonstrated that BDDN maintained a superior and more stable AUC compared to glasso, particularly under small sample size conditions.

Discussion

We propose a Bayesian framework to make inference on dynamic differential networks in protein data that are measured across time. Our approach enables the identification of dynamic changes in conditional dependencies among proteins, given all other proteins, in response to drug treatment, providing a flexible and statistically rigorous tool for network-based analysis.

We applied our method to the Cancer Perturbed Proteomics Atlas (CPPA) dataset, with a specific focus on responses to the targeted therapy drug LAPATINIB. By analyzing protein expression data collected at multiple time points, we identified several key protein pairs that exhibited significant changes in their conditional dependencies. These time-dependent interaction changes likely reflect the underlying molecular mechanisms and biological pathways involved in the cellular response to LAPATINIB treatment.

Our Bayesian analytical framework is inherently flexible, enabling its application to diverse covariate types beyond time, a wide range of other omics data, and integration of additional layers of biological or clinical information. By expanding x_i in Equation (1), we can readily incorporate multiple covariates. For example, drug dosage can be integrated as $\mathrm{x}_i = (1, d_i, time_i, dose_i)^{\mathrm{T}}$, where d_i is a binary indicator that represents treatment status (1 for the treatment group and 0 for the control group), allowing the model to simultaneously account for temporal and dosage effects. We further demonstrate that BDDN is naturally generalized to complex designs with uneven time intervals, multiple treatments, and subject covariates by defining time- and covariate-specific vectors x_i

and computing $\mathrm{R}(\mathrm{x}_i)$. Illustrative formulas and examples are provided in Supplementary Section 6.

We acknowledge that the inferred network edges represent statistical associations derived de novo and may not always correspond to direct physical protein-protein interactions-a characteristic inherent to all network inference approaches. To address this limitation and enhance the biological interpretability of our inferred networks, a promising direction for future research is the integration of prior biological knowledge. Specifically, future extensions could incorporate established protein interaction data from databases such as STRING [57] and BioGRID [58] as informative priors. Such integration would strategically guide the inference process toward known physical interactions while maintaining the framework's core ability to discover novel, context-specific dynamic relationships.

The quadratic specification represents a deliberate balance between capturing the observed nonlinear temporal patterns and preserving model stability given our sample size constraints. This approach avoids the potential overfitting risks associated with higher-order polynomial terms or more complex nonlinear specifications, while still accommodating the curved trajectories that characterize the biological responses in the CPPA data. Importantly, the covariance regression framework underlying BDDN maintains considerable flexibility for future extensions (e.g., basis expansion with splines) within the MCMC implementation without changing the overall inferential workflow.

Supplementary Information

The online version contains supplementary material available at https://doi.org/10.1186/s12859-026-06371-w.

Supplementary Material 1.

Author contributions

DL implemented the method, conducted the data analysis, and wrote the original draft of the manuscript. JK contributed to the data analysis, interpretation of the results, and manuscript editing. JP contributed to the study design and participated in manuscript editing. IHJ and MJH supervised the study and critically revised the manuscript. All authors read and approved the final version of the manuscript.

Funding

This work was partially supported by the National Research Foundation of Korea [grant number RS-2023-00217705 and RS-2024-00333701; Basic Science Research Program awarded to IHJ] and the National Research Foundation of Korea [grant number 2022R1A2C1091488 to MJH]. Dr. Jin and Dr. Ha are co-corresponding authors.

Data availability

The data supporting the findings of this study were obtained from the Cancer Perturbed Proteomics Atlas (CPPA) available at https://tcpaportal.org/cppa/#/. The datasets analyzed are publicly available and can be accessed from the CPPA portal under the relevant experimental conditions.

Code availability

All code for implementing the BDDN model and reproducing the results is available at: https://github.com/doyeonleee/BDDN.

Declarations

Ethics approval and consent to participate

Not applicable.

Consent for publication

Not applicable.

Competing interests

The authors declare that they have no Conflict of interest.

Received: 25 June 2025 / Accepted: 6 January 2026

Published online: 26 February 2026

References

1. Liebler DC. Introduction to proteomics: tools for the new biology. Totowa, New Jersey: Springer; 2001.
2. Alberts B, Johnson A, Lewis J, Raff M, Roberts K, Walter P. Proteins. 6th ed. New York: Garland Science; 2014. p. 166–72.
3. Dutta S, Ghosh S, Mishra A, Ghosh R. Oncoproteomics: insight into current proteomic technologies in cancer biomarker discovery and treatment. J Proteins Proteomics. 2023;14(1):1–24. https://doi.org/10.1007/s42485-022-00100-6.
4. Aebersold R, Mann M. Mass-spectrometric exploration of proteome structure and function. Nature. 2016;537(7620):347–55. https://doi.org/10.1038/nature19949.
5. Rodina A, Xu C, Digwal CS, Joshi S, Patel Y, Santhaseela AR, et al. Systems-level analyses of protein-protein interaction network dysfunctions via epichaperomics identify cancer-specific mechanisms of stress adaptation. Nat Commun. 2023;14(1):3742. https://doi.org/10.1038/s41467-023-39241-7.
6. Sajjad F, Jalal A, Jalal A, Mubeen H, Rizvi SZ, Nisa A, et al. Multi-omic analysis of dysregulated pathways in triple negative breast cancer. Asia Pac J Clin Oncol. 2024;20(4):450–62. https://doi.org/10.1111/ajco.14095.
7. Geffen Y, Anand S, Akiyama Y, Yaron TM, Song Y, Johnson JL, et al. Pan-cancer analysis of post-translational modifications reveals shared patterns of protein regulation. Cell. 2023;186(18):3945–67. https://doi.org/10.1016/j.cell.2023.07.013.
8. Lu Y, Chan Y-T, Tan H-Y, Li S, Wang N, Feng Y. Epigenetic regulation in human cancer: the potential role of epi-drug in cancer therapy. Mol Cancer. 2020;19:1–16. https://doi.org/10.1186/s12943-020-01197-3.
9. Jarnuczak AF, Najgebauer H, Barzine M, Kundu DJ, Ghavidel F, Perez-Riverol Y, et al. An integrated landscape of protein expression in human cancer. Scientific data. 2021;8(1):115. https://doi.org/10.1038/s41597-021-00890-2.
10. Rai A, Pradhan P, Nagraj J, Lohitesh K, Chowdhury R, Jalan S. Understanding cancer complexome using networks, spectral graph theory and multilayer framework. Sci Rep. 2017;7(1):41676. https://doi.org/10.1038/srep41676.
11. Kim M, Park J, Bouhaddou M, Kim K, Rojc A, Modak M, et al. A protein interaction landscape of breast cancer. Science. 2021;374(6563):3066. https://doi.org/10.1126/science.abf3066.
12. Farkash-Amar S, Eden E, Cohen A, Geva-Zatorsky N, Cohen L, Milo R, et al. Dynamic proteomics of human protein level and localization across the cell cycle. PLoS ONE. 2012;7(11):48722. https://doi.org/10.1371/journal.pone.0048722.
13. Islam MF, Hoque MM, Banik RS, Roy S, Sumi SS, Hassan FN, et al. Comparative analysis of differential network modularity in tissue specific normal and cancer protein interaction networks. J Clin Bioinform. 2013;3:1–23. https://doi.org/10.1186/2043-9113-3-19.
14. Zuo Y, Cui Y, Di Poto C, Varghese RS, Yu G, Li R, et al. Indeed: integrated differential expression and differential network analysis of omic data for biomarker discovery. Methods. 2016;111:12–20. https://doi.org/10.1016/j.ymeth.2016.08.015.
15. Archer TC, Fertig EJ, Gosline SJC, Hafner M, Hughes SK, Joughin BA, et al. Systems approaches to cancer biology. Can Res. 2016;76(23):6774–7. https://doi.org/10.1158/0008-5472.CAN-16-2961.
16. Ideker T, Krogan NJ. Differential network biology. Mol Syst Biol. 2012;8(1):565. https://doi.org/10.1038/msb.2011.99.
17. Tu J-J, Ou-Yang L, Zhu Y, Yan H, Qin H, Zhang X-F. Differential network analysis by simultaneously considering changes in gene interactions and gene expression. Bioinformatics. 2021;37(23):4414–23. https://doi.org/10.1093/bioinformatics/btab502.
18. Guzzi PH, Roy A, Milano M, Veltri P. Non parametric differential network analysis: a tool for unveiling specific molecular signatures. BMC Bioinform. 2024;25(1):359. https://doi.org/10.1186/s12859-024-05969-2.
19. Song W-M, Elmas A, Farias R, Xu P, Zhou X, Hopkins B, et al. Multiscale protein networks systematically identify aberrant protein interactions and oncogenic regulators in seven cancer types. J Hematol Oncol. 2023;16(1):120. https://doi.org/10.1186/s13045-023-01517-2.
20. Lapcik P, Stacey RG, Potesil D, Kulhanek P, Foster LJ, Bouchal P. Global interactome mapping reveals pro-tumorigenic interactions of nf-κb in breast cancer. Molecul Cell Proteomics. 2024;23(4):100744. https://doi.org/10.1016/j.mcpro.2024.100744.
21. Tesson BM, Breitling R, Jansen RC. Diffcoex: a simple and sensitive method to find differentially coexpressed gene modules. BMC Bioinform. 2010;11:1–9. https://doi.org/10.1186/1471-2105-11-497.
22. Amar D, Safer H, Shamir R. Dissection of regulatory networks that are altered in disease via differential co-expression. PLoS Comput Biol. 2013;9(3):1002955. https://doi.org/10.1371/journal.pcbi.1002955.
23. He H, Cao S, Zhang J-G, Shen H, Wang Y-P, Deng H-W. A statistical test for differential network analysis based on inference of gaussian graphical model. Sci Rep. 2019;9(1):10863. https://doi.org/10.1038/s41598-019-47362-7.
24. Leng J, Wu L-Y. Importance-penalized joint graphical lasso (ipjgl): differential network inference via ggms. Bioinformatics. 2022;38(3):770–7. https://doi.org/10.1093/bioinformatics/btab751.
25. Xue S, Rogers LR, Zheng M, He J, Piermarocchi C, Mias GI. Applying differential network analysis to longitudinal gene expression in response to perturbations. Front Genet. 2022;13:1026487. https://doi.org/10.3389/fgene.2022.1026487.
26. Xu T, Ou-Yang L, Yan H, Zhang X-F. Time-varying differential network analysis for revealing network rewiring over cancer progression. IEEE/ACM Trans Comput Biol Bioinf. 2019;18(4):1632–42. https://doi.org/10.1109/TCBB.2019.2949039.
27. Zhao W, Li J, Chen M-JM, Luo Y, Ju Z, Nesser NK, et al. Large-scale characterization of drug responses of clinically relevant proteins in cancer cell lines. Cancer Cell. 2020;38(6):829–43. https://doi.org/10.1016/j.ccell.2020.10.008.
28. Coarfa C, Grimm SL, Rajapakshe K, Perera D, Lu H-Y, Wang X, et al. Reverse-phase protein array: technology, application, data processing, and integration. J Biomol Tech JBT. 2021;32(1):15. https://doi.org/10.7171/jbt.21-3202-001.
29. Johnston S, Leary A. Lapatinib: a novel egfr/her2 tyrosine kinase inhibitor for cancer. Drugs Today (Barc). 2006;42(7):441–53. https://doi.org/10.1358/dot.2006.42.7.985637.
30. Valabrega G, Capellero S, Cavalloni G, Zaccarello G, Petrelli A, Migliardi G, et al. Her2-positive breast cancer cells resistant to trastuzumab and lapatinib lose reliance upon her2 and are sensitive to the multitargeted kinase inhibitor sorafenib. Breast Cancer Res Treat. 2011;130:29–40. https://doi.org/10.1007/s10549-010-1281-5.
31. Segovia-Mendoza M, González-González ME, Barrera D, Díaz L, García-Becerra R. Efficacy and mechanism of action of the tyrosine kinase inhibitors gefitinib, lapatinib and neratinib in the treatment of her2-positive breast cancer: preclinical and clinical evidence. Am J Cancer Res. 2015;5(9):2531.
32. Hoff PD, Niu X. A covariance regression model. Stat Sin. 2012;22(2):729–53. https://doi.org/10.5705/ss.2010.051.
33. Miller KS. On the inverse of the sum of matrices. Math Mag. 1981;54(2):67–72. https://doi.org/10.1080/0025570X.1981.11976898.
34. Jacques J, Preda C. Functional data clustering: a survey. Adv Data Anal Classif. 2014;8:231–55. https://doi.org/10.1007/s11634-013-0158-y.

35. Piegl L, Tiller W. B-Spline Basis Functions, pp. 47–79. Springer, Berlin, Heidelberg 1997. https://doi.org/10.1007/978-3-642-59223-2_2.
36. Mueller C, Liotta LA, Espina V. Reverse phase protein microarrays advance to use in clinical trials. Mol Oncol. 2010;4(6):461–81. https://doi.org/10.1016/j.molonc.2010.09.003.
37. Sankpal UT, Abdelrahim M, Connelly SF, Lee CM, Madero-Visbal R, Colon J, et al. Small molecule tolfenamic acid inhibits pc-3 cell proliferation and invasion in vitro, and tumor growth in orthotopic mouse model for prostate cancer. Prostate. 2012;72(15):1648–58. https://doi.org/10.1002/pros.22518.
38. Modesitt SC, Parsons SJ. In vitro and in vivo histone deacetylase inhibitor therapy with vorinostat and paclitaxel in ovarian cancer models: does timing matter? Gynecol Oncol. 2010;119(2):351–7. https://doi.org/10.1016/j.ygyno.2010.06.030.
39. Tang L, Wang Y, Strom A, Gustafsson JÅ, Guan X. Lapatinib induces p27kip1-dependent g_1 arrest through both transcriptional and post-translational mechanisms. Cell Cycle. 2013;12(16):2665–74. https://doi.org/10.4161/cc.25728.
40. Leung W-Y, Roxanis I, Sheldon H, Buffa FM, Li J-L, Harris AL, et al. Combining lapatinib and pertuzumab to overcome lapatinib resistance due to nrg1-mediated signalling in her2-amplified breast cancer. Oncotarget. 2015;6(8):5678. https://doi.org/10.18632/oncotarget.3296.
41. Vogel C, Chan A, Gril B, Kim S-B, Kurebayashi J, Liu L, et al. Management of erbb2-positive breast cancer: insights from preclinical and clinical studies with lapatinib. Jpn J Clin Oncol. 2010;40(11):999–1013. https://doi.org/10.1093/jjco/hyq084.
42. Cheng X. A comprehensive review of her2 in cancer biology and therapeutics. Genes. 2024;15(7):903. https://doi.org/10.3390/genes15070903.
43. Markman B, Dienstmann R, Tabernero J. Targeting the pi3k/akt/mtor pathway-beyond rapalogs. Oncotarget. 2010;1(7):530. https://doi.org/10.18632/oncotarget.188.
44. Eichhorn P, Gili M, Scaltriti M, Serra V, Guzman M, Nijkamp W, et al. Phosphatidylinositol 3-kinase hyperactivation results in lapatinib resistance that is reversed by the mtor/phosphatidylinositol 3-kinase inhibitor nvp-bez235. Can Res. 2008;68(22):9221–30. https://doi.org/10.1158/0008-5472.CAN-08-1740.
45. Mukherjee R, Vanaja KG, Boyer JA, Gadal S, Solomon H, Chandarlapaty S, et al. Regulation of pten translation by pi3k signaling maintains pathway homeostasis. Mol Cell. 2021;81(4):708–23. https://doi.org/10.1016/j.molcel.2021.01.033.
46. Casamayor A, Morrice NA, Alessi DR. Phosphorylation of ser-241 is essential for the activity of 3-phosphoinositide-dependent protein kinase-1: identification of five sites of phosphorylation in vivo. Biochem J. 1999;342(2):287–92. https://doi.org/10.1042/bj3420287.
47. Imami K, Sugiyama N, Imamura H, Wakabayashi M, Tomita M, Taniguchi M, et al. Temporal profiling of lapatinib-suppressed phosphorylation signals in egfr/her2 pathways. Mol Cell Proteomics. 2012;11(12):1741–57. https://doi.org/10.1074/mcp.M112.019919.
48. Xiao L, Wang YC, Li WS, Du Y. The role of mtor and phospho-p70s6k in pathogenesis and progression of gastric carcinomas: an immunohistochemical study on tissue microarray. J Exp Clin Cancer Res. 2009;28:1–9. https://doi.org/10.1186/1756-9966-28-152.
49. Duchnowska R, Wysocki PJ, Korski K, Czartoryska-Arłukowicz B, Niwińska A, Orlikowska M, et al. Immunohistochemical prediction of lapatinib efficacy in advanced her2-positive breast cancer patients. Oncotarget. 2015;7(1):550. https://doi.org/10.18632/oncotarget.6375.
50. Rozengurt E, Soares HP, Sinnet-Smith J. Suppression of feedback loops mediated by pi3k/mtor induces multiple overactivation of compensatory pathways: an unintended consequence leading to drug resistance. Mol Cancer Ther. 2014;13(11):2477–88. https://doi.org/10.1158/1535-7163.MCT-14-0330.
51. Stuhlmiller TJ, Miller SM, Zawistowski JS, Nakamura K, Beltran AS, Duncan JS, et al. Inhibition of lapatinib-induced kinome reprogramming in erbb2-positive breast cancer by targeting bet family bromodomains. Cell Rep. 2015;11(3):390–404. https://doi.org/10.1016/j.celrep.2015.03.037.
52. Garrett JT, Olivares MG, Rinehart C, Granja-Ingram ND, Sánchez V, Chakrabarty A, et al. Transcriptional and post-translational up-regulation of her3 (erbb3) compensates for inhibition of the her2 tyrosine kinase. Proc Natl Acad Sci. 2011;108(12):5021–6. https://doi.org/10.1073/pnas.1016140108.
53. O'Connell K, Li J, Engler F, Hennessy K, O'Neill F, Straubinger RM, et al. Determination of the proteomic response to lapatinib treatment using a comprehensive and reproducible ion-current-based proteomics strategy. J Proteomics Genomics Res. 2013;1(3):27. https://doi.org/10.14302/issn.2326-0793.jpgr-13-257.
54. Ma C, Zuo W, Wang X, Wei L, Guo Q, Song X. Lapatinib inhibits the activation of nf-κb through reducing phosphorylation of iκb-α in breast cancer cells. Oncol Rep. 2013;29(2):812–8. https://doi.org/10.3892/or.2012.2159.
55. Ha MJ, Baladandayuthapani V, Do K-A. Dingo: differential network analysis in genomics. Bioinformatics. 2015;31(21):3413–20. https://doi.org/10.1093/bioinformatics/btv406.
56. Friedman J, Hastie T, Tibshirani R. Sparse inverse covariance estimation with the graphical lasso. Biostatistics. 2008;9(3):432–41.
57. Szklarczyk D, Franceschini A, Wyder S, Forslund K, Heller D, Huerta-Cepas J, et al. String v10: protein-protein interaction networks, integrated over the tree of life. Nucleic Acids Res. 2015;43(D1):447–52.
58. Chatr-Aryamontri A, Breitkreutz B-J, Oughtred R, Boucher L, Heinicke S, Chen D, et al. The biogrid interaction database: 2015 update. Nucleic Acids Res. 2015;43(D1):470–8.

Publisher's Note